

# Non-encapsulation approach for high-performance Li-S batteries through controlled nucleation and growth

Huilin Pan<sup>1,2</sup>, Junzheng Chen<sup>1,2</sup>, Ruiguo Cao<sup>1,2</sup>, Vijay Murugesan<sup>1,2</sup>, Nav Nidhi Rajput<sup>3</sup>, Kee Sung Han<sup>1,4</sup>, Kristin Persson<sup>3,5</sup>, Luis Estevez<sup>2</sup>, Mark H. Engelhard<sup>4</sup>, Ji-Guang Zhang<sup>1,2</sup>, Karl T. Mueller<sup>1,6</sup>, Yi Cui<sup>7</sup>, Yuyan Shao<sup>1,2\*</sup> and Jun Liu<sup>1,2\*</sup>

**High-surface-area, nanostructured carbon is widely used for encapsulating sulfur and improving the cyclic stability of Li-S batteries, but the high carbon content and low packing density limit the specific energy that can be achieved. Here we report an approach that does not rely on sulfur encapsulation. We used a low-surface-area, open carbon fibre architecture to control the nucleation and growth of the sulfur species by manipulating the carbon surface chemistry and the solvent properties, such as donor number and Li<sup>+</sup> diffusivity. Our approach facilitates the formation of large open spheres and prevents the production of an undesired insulating sulfur-containing film on the carbon surface. This mechanism leads to ~100% sulfur utilization, almost no capacity fading, over 99% coulombic efficiency and high energy density (1,835 Wh kg<sup>-1</sup> and 2,317 Wh l<sup>-1</sup>). This finding offers an alternative approach for designing high-energy and low-cost Li-S batteries through controlling sulfur reaction on low-surface-area carbon.**

The growing demand for high-energy-density energy storage for transportation and the grid has stimulated extensive research beyond Li-ion battery technologies<sup>1</sup>. Among these, Li-S batteries have attracted wide attention because of their high theoretical energy<sup>2,3</sup>. Despite intensive research, there are still significant obstacles to developing practical Li-S batteries<sup>4–6</sup>. The major challenges arise from the highly insulating S/Li<sub>2</sub>S and the dissolution of intermediate polysulfides during charge/discharge<sup>7,8</sup>. The former results in low sulfur utilization<sup>9,10</sup> and the latter causes low coulombic efficiency and rapid capacity fading in Li-S batteries<sup>7</sup>.

Most current efforts on Li-S batteries are devoted to nanostructuring appropriate sulfur cathode architectures to reduce the dissolution of polysulfides. A commonly employed strategy is to confine polysulfides within the pores or onto high-surface-area host materials (encapsulation). These host materials include mesoporous carbon<sup>11</sup>, hollow carbon spheres<sup>12</sup>, graphene<sup>13,14</sup>, hollow carbon nanofibres<sup>15,16</sup>, transition metal oxide or carbide<sup>17,18</sup> and conductive polymers<sup>19</sup>. Although the encapsulation approach has been proved to be effective to alleviate the dissolution of polysulfides thus enabling extended cyclic life, the typical sulfur utilization is only 35% to 70%<sup>20–23</sup> and the large amount of high-surface-area matrix significantly decreases the achievable energy density. The low sulfur utilization indicates a substantial amount of inactive S/Li<sub>2</sub>S (refs 24,25). This could be due to the electric passivation of the sulfur cathode by the uncontrollable aggregation of poorly conductive S/Li<sub>2</sub>S in the cathode<sup>26</sup>. Such passivation inhibits charge transfer across the sulfur electrode/electrolyte interface where the sulfur reactions occur and leads to gradual capacity loss during cycling<sup>27</sup>.

Therefore, it is desirable to develop alternative approaches that do not depend on high-surface-area carbon. To accomplish this goal, it is important to understand and control the S/Li<sub>2</sub>S precipitation process in the cathode during charge/discharge<sup>27–29</sup>. This is extremely crucial to achieving high reversible capacity and enhancing the kinetics of sulfur reactions at the electrode/electrolyte interface<sup>27</sup>. Studies on the growth and precipitation of Li<sub>2</sub>O<sub>2</sub> in Li–O<sub>2</sub> batteries have provided important guidance to the design of the interface between the oxygen cathode and electrolyte<sup>30,31</sup>. In the Li–S system, there have been numerous studies on tuning carbon matrix surface chemistry to improve its binding towards sulfur species, but these approaches still depend on high-surface-area carbon substrates and there is little knowledge to aid in the understanding and control of the growth of sulfur species.

Here we use low-surface-area carbon material, carbon fibres (CFs), to control the polysulfide deposition processes. Two different deposition pathways for sulfur species are demonstrated (Fig. 1). One involves a surface electrochemical reaction mechanism that produces a continuous S/Li<sub>2</sub>S film, but the insulating nature of the S/Li<sub>2</sub>S film limits the charge transport across the film. The traditional approach of encapsulating sulfur into high-surface-area carbon by the melt-diffusion method usually belongs to the continuous film growth mechanism. The second is the growth of S/Li<sub>2</sub>S particles through a carbon surface- and solution-mediated electrochemical process in appropriate solvents, such as DOL:DME, in which the nucleation and growth of sulfur species heterogeneously occur instead of even film-like precipitation. This pathway promotes the growth of micro-sized ‘flower-like’ S/Li<sub>2</sub>S

<sup>1</sup>Joint Center for Energy Storage Research (JCESR), Pacific Northwest National Laboratory, Richland, WA 99352, USA. <sup>2</sup>Energy and Environmental Directorate, Pacific Northwest National Laboratory, Richland, WA 99352, USA. <sup>3</sup>Lawrence Berkeley National Laboratory, Berkeley, CA 94720, USA.

<sup>4</sup>Environmental Molecular Sciences Laboratory, Pacific Northwest National Laboratory, Richland, WA 99352, USA. <sup>5</sup>Department of Materials Science and Engineering, University of California-Berkeley, Berkeley, CA 94720, USA. <sup>6</sup>Physical and Computational Sciences Directorate, Pacific Northwest National Laboratory, Richland, WA 99352, USA. <sup>7</sup>Department of Materials Science and Engineering, Stanford University, Stanford, CA 94305, USA.

\*e-mail: [yuyan.shao@pnnl.gov](mailto:yuyan.shao@pnnl.gov); [jun.liu@pnnl.gov](mailto:jun.liu@pnnl.gov)

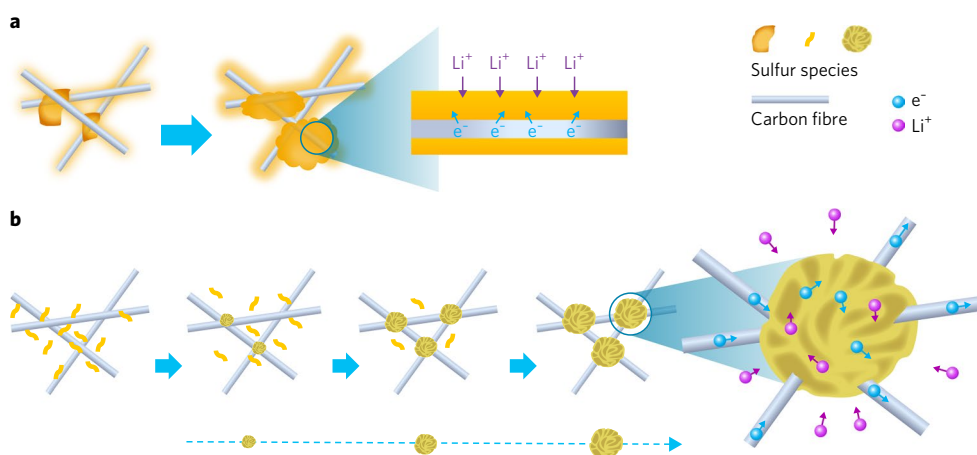


**Fig. 1 | Two different growth pathways of sulfur species during electrochemical process in Li-S batteries.** **a**, In the traditional melt-diffusion encapsulation approach (MD-encapsulation approach), the sulfur species are involved in a 2D surface electrochemical reaction mechanism that produces a continuous insulating S/Li<sub>2</sub>S film, which limits the charge transport across the insulating film and causes passivation. **b**, In the non-encapsulation approach the sulfur species are deposited onto the carbon fibres from an electrochemical precipitation process from the Li<sub>2</sub>S<sub>8</sub> catholyte. The heterogeneous nucleation leads to the formation of 3D ‘flower-like’ particles that generate a mixed conducting network for Li<sup>+</sup> and electrons. The arrows indicate the possible moving directions of Li<sup>+</sup> and electrons.

agglomerates within the electronically conducting CF architecture. These large S/Li<sub>2</sub>S agglomerates efficiently fill up the void space in the CF electrode, leading to ~100% sulfur utilization, high energy density (1,835 Wh kg<sup>-1</sup> and 2,317 Wh l<sup>-1</sup> based on the overall cathode), high coulombic efficiency and good electrochemical properties. The investigation of important factors, such as the surface properties of the carbon host, the donor number (DN) of the solvents and the Li<sup>+</sup> ion diffusivity, that influence the nucleation and growth of Li<sub>2</sub>S reveals a surface- and solution-mediated nucleation process.

### Growth pathways for S/Li<sub>2</sub>S in Li-S batteries

Low-surface-area CF (~17 m<sup>2</sup> g<sup>-1</sup>, Supplementary Fig. 1) is used as the host material for the sulfur cathodes. Two different electrode fabrication processes are employed for comparison. One is using the traditional approach of encapsulating solid sulfur onto the CF surface by the melt-diffusion method (MD-Encap-S/CF)<sup>2</sup>. The other is to deposit sulfur species onto the CF matrix from Li<sub>2</sub>S<sub>8</sub> catholyte through an in situ electrochemical process (Non-Encap-S/CF). Note that both sulfur electrodes were processed with similar areal sulfur loading of ~2.5 mg cm<sup>-2</sup> (60 wt% sulfur for MD-Encap-S/CF and 64–67 wt% sulfur for Non-Encap-S/CF; see details in Methods) and the same amount of electrolyte. The galvanostatic charge–discharge curves of the Li–S cells with S/CF electrodes are shown in Fig. 2a,d. The traditional MD-Encap-S/CF electrode delivered only a limited capacity of about 600 mAh g<sup>-1</sup>, corresponding to a sulfur utilization of ~35% with a significant reduction in the second discharge plateau (Fig. 2a). The low discharge capacity is expected considering the low surface area of CFs and the poor reaction kinetics of conversion from short-chain polysulfides to insulating Li<sub>2</sub>S in the second discharge plateau<sup>2</sup>. In contrast, although using the same low-surface-area carbon host, almost 100% utilization of sulfur (1,632 mAh g<sup>-1</sup>) was obtained from the Non-Encap-S/CF electrode (Fig. 2d). The discharge plateaus in the voltage range of 2.4–2.2 V and 2.2–1.8 V correspond to the conversion from S<sub>8</sub> to Li<sub>2</sub>S<sub>4</sub> and Li<sub>2</sub>S<sub>4</sub> to Li<sub>2</sub>S, respectively, which present a theoretical ratio of about 1:3 in terms of the discharge capacity. In addition, the reversible areal capacity is about 3.75 mAh cm<sup>-2</sup> — more than two times higher than the MD-Encap-S/CF electrode and with much smaller overpotential.

Figure 2b,c,e,f shows scanning electron microscopy (SEM) images of the above two different sulfur electrodes in the first cycle. After discharge, uneven accumulation of discharge products onto the S/CF framework was observed for the MD-Encap-S/CF electrode (Fig. 2b). A higher-magnification SEM image in Fig. 2c indicates that the surface of the CFs is almost completely covered by electronically insulating discharge products (most likely Li<sub>2</sub>S, and to a lesser extent, unreacted poorly conducting sulfur and/or insoluble Li<sub>2</sub>S<sub>x</sub>). The subsequent formation of Li<sub>2</sub>S prefers to grow on the existing Li<sub>2</sub>S layer. This causes the increase in the thickness of the precipitation layer on the surface of the CF host, which has limited available surface area<sup>32</sup>. It will block the charge transfer between the CF framework and the Li<sub>2</sub>S/electrolyte interface at a certain thickness and hinder the continuous electrochemical transformation between S<sub>8</sub> and Li<sub>2</sub>S. The passivation by insulating Li<sub>2</sub>S in the cathode leads to poor reaction kinetics and largely reduced discharge capacity (particularly the second discharge plateau) and larger overpotential in the MD-Encap-S/CF electrode as shown in Fig. 2a.

For the Non-Encap-S/CF electrode, crystalline ‘flower-like’ Li<sub>2</sub>S agglomerate particles (Supplementary Fig. 2) were observed within the CF framework after discharge. Although the final discharge particles are almost 3–5 μm in diameter (Fig. 2e,f), they are in fact formed from thin-flake primary building blocks with electronically conductive CFs passing through the large particles, resulting in an open structure that favours both electron and ion transport. It should be noted that, in Li–O<sub>2</sub> batteries, large toroid-structured Li<sub>2</sub>O<sub>2</sub> benefits the large capacity rather than the thin conformal layer of Li<sub>2</sub>O<sub>2</sub> (refs<sup>30,33</sup>). We believe that the formation of ‘flower-like’ large Li<sub>2</sub>S agglomerates within the conducting CF framework is the reason for the high specific capacity and small overpotential (Fig. 2d). Furthermore, the large Li<sub>2</sub>S agglomerates do not depend on encapsulation; they efficiently fill up the void space in the hierarchically porous electrode, which significantly reduces the electrode porosity (Supplementary Fig. 3) and leads to almost a magnitude higher volumetric energy density in comparison with the traditional MD-Encap-S/CF composite electrodes (Supplementary Table 1). The electrode density of the Non-Encap-S/CF electrode (at discharge state) is 1.26 g cm<sup>-3</sup>, more than a factor of three higher than the traditional MD-Encap-S/CF electrode in this work. The obtained energy density of the Non-Encap-S/CF sulfur cathode

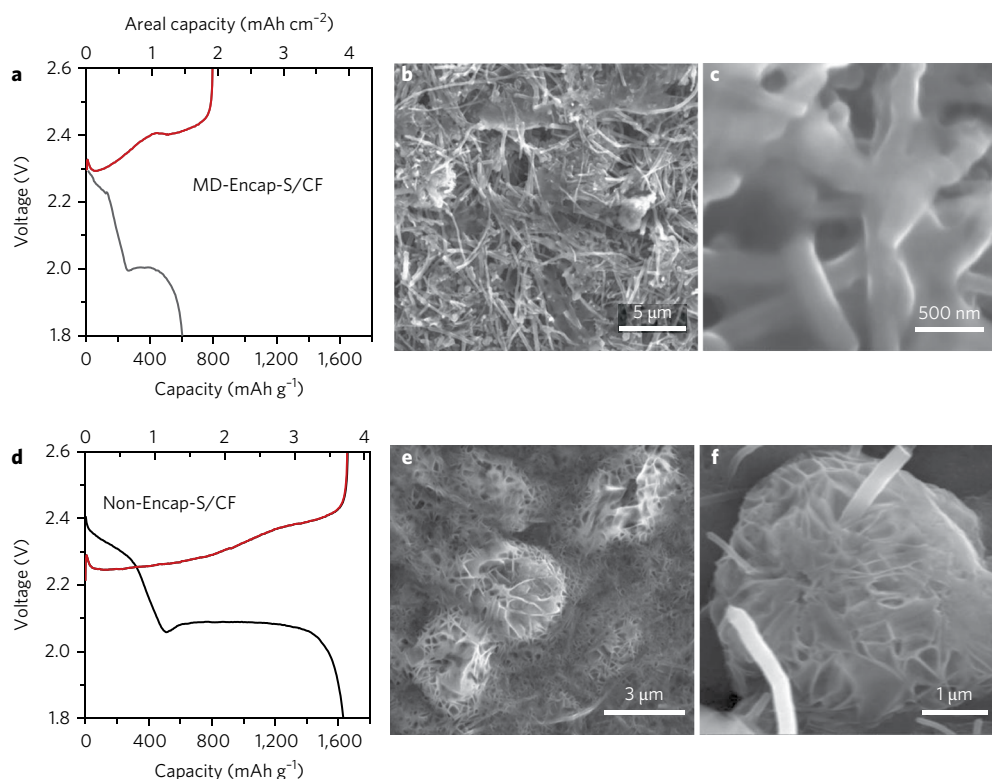


**Fig. 2 | Electrochemical profiles and the discharge product morphology of Li-S batteries with different electrode processes. a,b,c,** Charge (red) and discharge (black) curves in the second cycle for MD-Encap-S/CF (**a**) and SEM images obtained from MD-Encap-S/CF (**b,c**) at discharge state in the first cycle. **d,e,f,** Charge (red) and discharge (black) curves in the second cycle for Non-Encap-S/CF (**d**) and SEM images obtained from Non-Encap-S/CF (**e,f**) at discharge state in the first cycle. The electrolyte is 0.5 M LiTFSI/2wt% LiNO<sub>3</sub>/DOL:DME and C rate is 0.1C.

(at discharge state) is 1,835 Wh kg<sup>-1</sup> and 2,317 Wh l<sup>-1</sup> (based on the overall mass/volume of the cathode).

We studied the evolution of nucleation and growth of sulfur species on the CF surface (Supplementary Fig. 4). X-ray photoelectron spectroscopy of CFs suggests that certain functional groups induce the initial nucleation of sulfur particles on the surface (Supplementary Fig. 5). Sulfur species were first observed, particularly near the junctions of CFs. The subsequent growth of sulfur species indicates that the sulfur species prefer to grow on the formed sulfur, instead of an even coverage of the CF surface. During the discharge process, the nucleated sulfur particles grew to larger particles (3–5 μm) displaying an open (porous) structure and gradually filled up the CF host electrode. The ‘flower-like’ morphology is favoured by low current densities (Supplementary Fig. 6). At higher current densities, the Li<sub>2</sub>S particles retain the porous structure, but with smaller particle size. During the charge process, the morphology of sulfur species does not change much. It is likely that the heterogeneous nucleation and growth of large particles on the carbon surface reduces random precipitation, and provides a self-sustaining architecture to support the sulfur species. In addition, their dissolution kinetics is significantly suppressed due to the large particles size, resulting in high mechanical stability of large agglomerate of sulfur species in the electrode during the subsequent electrochemical reactions, which is also consistent with their excellent electrochemical performance.

The electrochemical behaviours of both CF-based electrodes with different morphology of sulfur species were evaluated in coin cells. The Non-Encap-S/CF electrode shows excellent rate capacity with low overpotential, achieving a high capacity of 1,500 mAh g<sup>-1</sup> at 0.2C, 1,400 mAh g<sup>-1</sup> at 0.5C and 1,300 mAh g<sup>-1</sup> at 1C (discharge cutoff voltage 1.7 V) as shown in Fig. 3a. Of note, the second discharge plateau does not degrade much in terms of either capac-

ity or voltage when increasing the current density. This suggests that the Non-Encap-S/CF electrode with micro-sized hierarchically porous agglomerates remains electrochemically active even under larger current densities. This is crucial to realize high capacity for practical Li-S batteries. In addition, the Non-Encap-S/CF electrode exhibits more stable cycling than the MD-Encap-S/CF electrode, and more than a factor of two higher sulfur utilization (Fig. 3b). Furthermore, Fig. 3c shows that the coulombic efficiency of the Non-Encap-S/CF electrode reaches >99% and retains >98.6% after 100 cycles as compared with the ~80% efficiency obtained for the MD-Encap-S/CF electrode with layer-like sulfur morphology. The high coulombic efficiency further indicates that the large ‘flower-like’ precipitation within the CF matrix provides a self-sustaining architecture to support the sulfur within the cathode and ensure reversible sulfur reactions by suppressing the polysulfide shuttle effect during cycling.

*Operando* electrochemical impedance spectroscopy (EIS) was used to investigate the underlying reasons for the remarkable performance difference of Li-S cells with different morphological control of deposited sulfur species in the cathode. The EIS measurements at different electrochemical states were recorded for both Non-Encap-S/CF|Li and MD-Encap-S/CF|Li cells during cycling (Fig. 4). They show similar shapes with two semi-circles located at high and low frequencies respectively (Supplementary Fig. 7), indicating comparable electrochemical processes in both CF-based electrodes. The semi-circles typically reveal the different electrochemical processes occurred inside the Li-S cells<sup>27</sup>. The obtained *operando* EIS from both Li-S cells were carefully analysed with equivalent circuit (Fig. 4 inset) during cycling. The  $R_s$  corresponds to the system ohmic resistance of the cells. The  $R_1/CPE_1$  from the first semi-circle in the high-frequency range is assigned to the resistance and capacitance of the solid electrolyte interphase

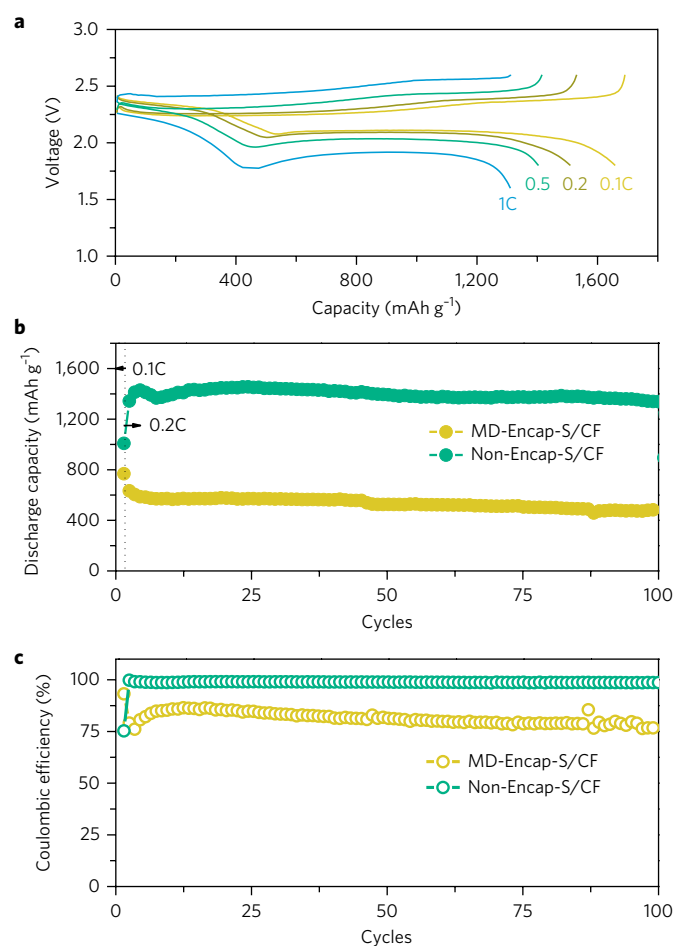


**Fig. 3 | Electrochemical performances of sulfur electrodes.** **a**, The rate performance of the Non-Encap-S/CF electrode. **b,c**, Comparisons of cycling and coulombic efficiency of Non-Encap-S/CF and MD-Encap-S/CF electrodes at 0.2C. The areal capacity of the sulfur electrodes in **b,c** is  $-1.5 \text{ mAh cm}^{-2}$ .

(SEI) layer on sulfur cathode and Li metal side<sup>27</sup>. The  $R_{ct}/CPE_2$  from the second semi-circle in the low-frequency range is attributed to the charge transfer process from the interface of the sulfur cathode to the electrolyte<sup>34,35</sup>. The stable and low resistance (green curves) in the Non-Encap-S/CF|Li cell indicates a favourable and sustainable conducting network and charge transfer at the sulfur electrode interface. Even after 20 cycles at large areal capacity ( $\sim 4 \text{ mAh cm}^{-2}$ ), the  $R_s$ ,  $R_1$  and  $R_{ct}$  in the Non-Encap-S/CF|Li cell remain similar to those for the initial cycles. In contrast, much higher resistances are observed in the MD-Encap-S/CF | Li cell (yellow curves), along with a gradual increase during cycling. More importantly, the huge surge in charge transfer resistance at the interface in the MD-Encap-S/CF electrode after extended cycles further indicates the dramatically destructive effect of layer precipitation. This finally causes uncontrollable accumulation and detachment of sulfur species in the sulfur cathode even in the case of encapsulating sulfur into a high-surface-area carbon host (Supplementary Fig. 8)<sup>26</sup>. On the basis of the above discussion, the EIS results clearly explain the fundamental reasons for the much higher sulfur utilization and enhanced reaction kinetics in the non-encapsulation sulfur electrodes, that is, the stable and low-resistance interfaces.

### Factors controlling nucleation and growth of sulfur species

Our study suggests that the nucleation and growth pathway of sulfur species plays an important role in influencing the electrochemical

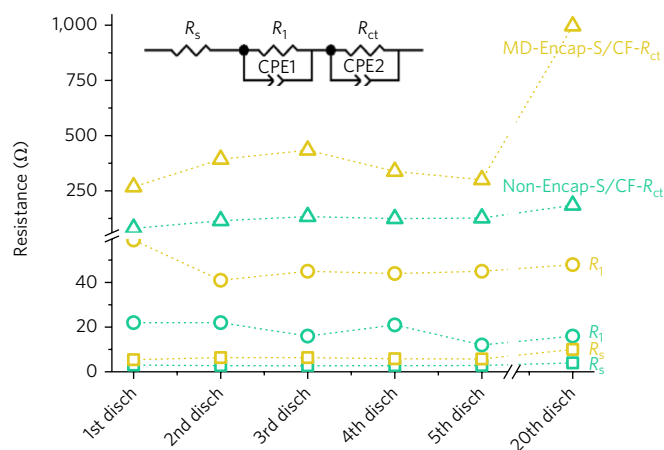


**Fig. 4 | Operando EIS analysis of Non-Encap-S/CF|Li and MD-Encap-S/CF|Li cells during cycling.** The green and yellow curves represent the variation of impedance from Non-Encap-S/CF|Li and MD-Encap-S/CF|Li cells during cycling, respectively. The inset is the equivalent circuit used to fit the obtained EIS spectra. The x axis indicates the discharge status with cycling.

performance of Li-S batteries. The identification of factors controlling the nucleation phenomena of sulfur species is instructive to non-encapsulation sulfur cathode design that can avoid the use of high-surface-area, porous host materials.

The surface chemistry of the carbon host is an important factor affecting the nucleation and growth of sulfur species by tailoring the nucleation barriers on different substrate surfaces<sup>36</sup>. We investigated the effect of CF surface chemistry in the LiTFSI/DOL:DME electrolyte system. The CF surface was functionalized with O groups (C=O, C-O and O-C=O) using O<sub>2</sub> plasma treatment as reported in the literature to enhance the nucleation on the surface (Fig. 5a)<sup>37</sup>. Surprisingly, the first electrochemical deposition of Li<sub>2</sub>S onto the O-functionalized CF electrode (red line) shows increased overpotential and decreased capacity compared with the CF electrode without functionalization (grey line) in Fig. 5b, suggesting that the enhanced nucleation is not favourable for the non-encapsulation approach. The SEM image shows no change on the CF surface treated with O<sub>2</sub> plasma (Fig. 5c). During discharge, O groups on the CF surface have a large effect on the morphology of electrochemically formed Li<sub>2</sub>S. With shallow discharge of Li<sub>2</sub>S<sub>8</sub> catholyte, a smooth layer is formed on O<sub>2</sub>-plasma-treated CFs (Fig. 5d). It is reasonable to suggest that O groups on the CFs serve as nucleation sites for uniform electrochemical coating of sulfur species onto the CF surface compared with non-functionalized CF. For the full discharge, Li<sub>2</sub>S layers cover almost the entire carbon surface and extend to form porous Li<sub>2</sub>S structures at the junctions of the CFs (Fig. 5e). Although a high capacity of  $>1,500 \text{ mAh g}^{-1}$  is shown for the O<sub>2</sub>-plasma-treated CF, the Li-S cell shows significantly increased overpotential and poor cyclic stability (Supplementary Fig. 9). The strong chemical interaction between the host material and polysulfides is commonly believed to be beneficial for trapping polysulfides<sup>18,22,38</sup>, but our results indicate that the strong interaction induces the layer-like coverage of insulating sulfur species on the carbon (Supplementary Figs. 9–10). A balanced approach is needed to induce the nucleation on the surface, but not causing surface passivation by the deposited particles.

To further explore the fundamental mechanism of Li<sub>2</sub>S nucleation and growth from Li<sub>2</sub>S<sub>8</sub> catholyte, morphologies of Li<sub>2</sub>S obtained across a range of solvents with different donor number (DN)<sup>39</sup> are shown in Fig. 6. The cells with different electrolytes were discharged under the same conditions, showing substantially

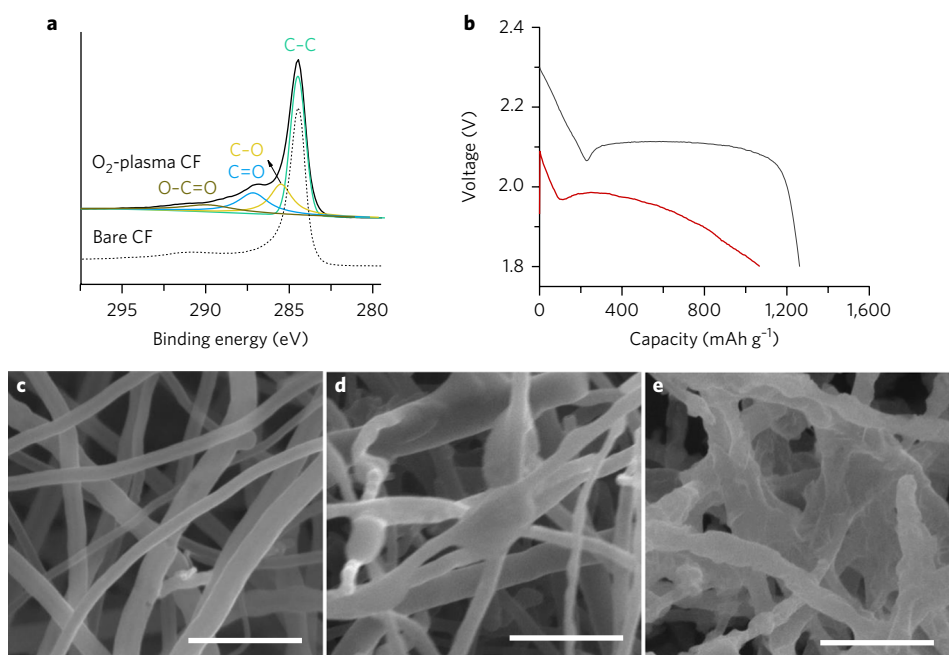


**Fig. 5 | Characterization of O<sub>2</sub>-plasma-treated CF electrodes.** **a**, The XPS of CF before and after 20 min of O<sub>2</sub> plasma treatment. (The black curves are the measured spectra; the coloured curves are fitting spectra; see details in Methods.) **b**, Comparison of electrochemical deposition of Li<sub>2</sub>S from 4.8 M Li<sub>2</sub>S<sub>8</sub> catholyte before (grey line) and after (red line) treatment in the first discharge. **c–e**, SEM images of O<sub>2</sub>-plasma-treated CF and the Li<sub>2</sub>S morphologies on discharge with shallow and full discharge respectively with O<sub>2</sub>-plasma-treated CF electrodes at 0.1C. Scale bars, 1 μm.

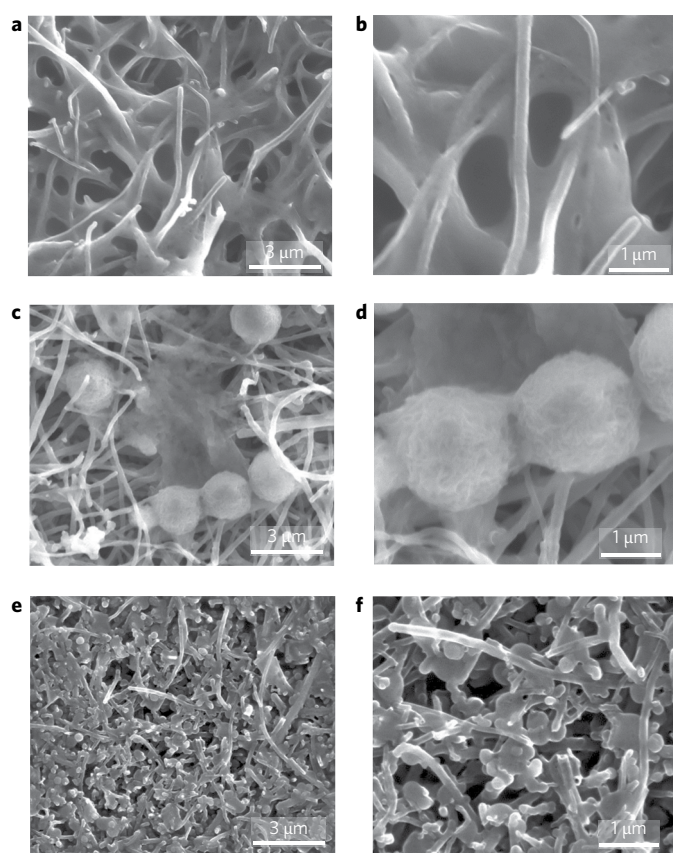


**Fig. 6 | SEM images showing the Li<sub>2</sub>S morphologies on discharge with 1M Li<sub>2</sub>S<sub>8</sub> in different solvents.** **a, b**, Full discharge in TMS. **c, d**, Full discharge in DOL:DME. **e, f**, Full discharge in DMSO.

varying morphologies of Li<sub>2</sub>S. Li<sub>2</sub>S film formation is observed in low-DN solvent of tetramethylene sulfone (TMS, DN=14.8); large particles are observed in intermediate-DN solvents (DOL:DME, DN=~20). The high-DN dimethylsulfoxide (DMSO, DN=30) results in Li<sub>2</sub>S particles but with much reduced particle size (~400 nm). These results indicate that solvents affect the Li–S discharge process and the formation pathway of sulfur species. The different pathways in different solvents could be explained by how nucleation occurs<sup>40</sup>. Higher-DN solvents provide strong solvation of Li<sup>+</sup> or Li<sup>+</sup>-containing species (such as Li<sub>2</sub>S<sub>x</sub>) and higher solubility of Li<sub>2</sub>S<sub>x</sub>, thus would probably favour the formation of Li<sub>2</sub>S particles from solution instead of forming a film through soluble polysulfides during discharge. Similar behaviour is observed for the formation of Li<sub>2</sub>O<sub>2</sub> in aprotic solvents in Li–air batteries where a higher DN solvent with larger Li<sub>2</sub>O<sub>2</sub> solubility favours large-particle formation of Li<sub>2</sub>O<sub>2</sub> (ref. 41). However, the nucleation barrier is also higher if the solvation interaction is too strong, resulting in the formation of very small particles. In a solvent with a low DN number, polysulfides readily precipitate and coat the carbon surfaces. For solvents with intermediate DN numbers, the polysulfide has appropriate solubility balancing the nucleation of the polysulfide particles in the solution with the subsequent particle growth. We note that the trend of discharge capacities from the different Li<sub>2</sub>S<sub>x</sub>/Li<sub>2</sub>S formation pathway in different electrolytes is consistent with our discussion that large particle precipitation of Li<sub>2</sub>S leads to higher capacity (Supplementary Figs. 11–13). In low-DN solvent, the voltage decays faster, leading to low discharge capacity, due to the insulating Li<sub>2</sub>S film covering the electrode. DOL:DME with intermediate DN not only shows the highest capacities, but also provides excellent kinetics and stability of sulfur reactions as shown in Fig. 3.

We further used classical molecular dynamics (MD) simulation and pulsed field gradient nuclear magnetic resonance spectroscopy (NMR) to provide additional evidence for the nature of solvent interactions and the mobility of Li<sup>+</sup> cations in different electrolytes at the molecular scale (Fig. 7). Their influence on the

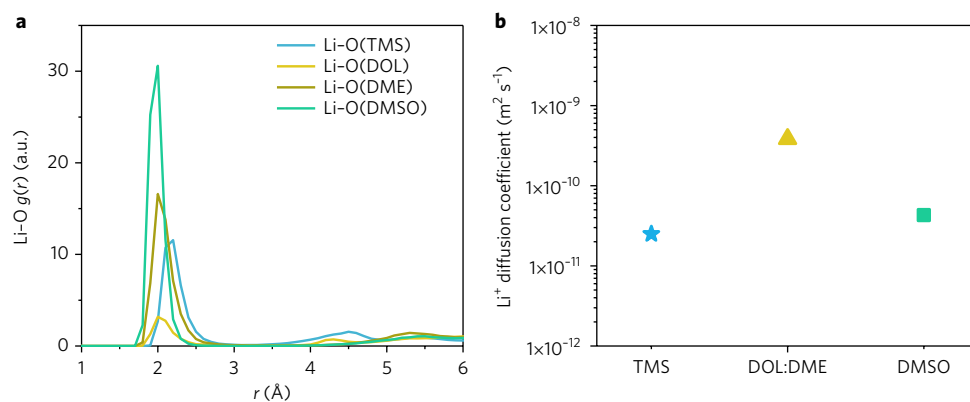


**Fig. 7 | MD simulation and experimental diffusion measurements in different solvent systems.** **a**, MD simulation of Li-O (O from solvent) radical distribution functions  $g(r)$  in different electrolytes with 0.25 M  $\text{Li}_2\text{S}_8$  and 1 M LiTFSI. **b**,  $\text{Li}^+$  cation diffusion coefficients for 1 M  $\text{Li}_2\text{S}_8$ -containing electrolytes: 1 M LiTFSI dissolved in TMS, 1 M LiTFSI dissolved in DOL:DME and 2 M LiTFSI dissolved in DMSO at 20 °C.

growth pathway of sulfur species during electrochemical deposition was also investigated. The radial distribution function from MD simulation shows a shorter bond length between  $\text{Li}^+$  and the solvent oxygen for the higher-DN solvents, indicating stronger solvation (Fig. 7a). Hence, DMSO results in the highest nucleation overpotential for  $\text{Li}_2\text{S}$  during the discharge (Supplementary Fig. 11), yielding small nucleation size and large nucleation density<sup>42</sup>. In DOL:DME and TMS solvents with weaker  $\text{Li}^+$  solvation, the nucleation of  $\text{Li}_2\text{S}$  particle size increases consequently, whereas the diffusion of  $\text{Li}^+$  dominates the following growth of  $\text{Li}_2\text{S}$  from the solution (Fig. 7b). The largest  $\text{Li}^+$  diffusion coefficient in DOL:DME ( $3.84 \times 10^{-10} \text{ m}^2 \text{ s}^{-1}$ ) accounts for the observed large particles of  $\text{Li}_2\text{S}$  in DOL:DME during the discharge in Fig. 6c,d and excellent reaction kinetics as discussed above. The relative smaller  $\text{Li}^+$  diffusion coefficient in DMSO restricts the growth of small nucleation seeds of  $\text{Li}_2\text{S}$  and causes the observed morphology of small particles in DMSO solvents in Fig. 6e,f. The most sluggish  $\text{Li}^+$  diffusion in TMS ( $2.5 \times 10^{-11} \text{ m}^2 \text{ s}^{-1}$ ) even limits the three-dimensional (3D) growth of  $\text{Li}_2\text{S}$ , forming a 2D layer-like morphology covered on the CF substrate as observed in Fig. 6a,b<sup>43</sup>. Nevertheless, the nucleation and growth process of sulfur species during electrochemical reactions is very complicated, which may also be affected by other factors, such as temperature, pressure and chemical equilibrium of different chain lengths of intermediate polysulfides. Further detailed investigation is still needed to understand the mechanisms.

## Conclusions

We demonstrated the potential for a non-encapsulation approach for high-performance Li-S batteries using low-surface-area carbon. Almost 100% sulfur utilization is obtained when the sulfur species form a micro-sized ‘flower-like’ structure on the low-surface-area carbon fibres. It also leads to high energy density and good electrochemical properties. The relationship between  $\text{Li}_2\text{S}$  growth mode/morphology and the surface chemistry of the carbon host and the properties of electrolytes, such as the DN of the solvent and  $\text{Li}^+$  diffusivity, has been identified. The growth of large S/ $\text{Li}_2\text{S}$  ‘flower-like’ agglomerates is related to a surface- and solution-mediated electrochemical process in intermediate-DN solvent driven by the high concentration of soluble polysulfides and fast  $\text{Li}^+$  diffusion in the catholyte. Strong interaction between the host material and polysulfides induces a layer-like growth of sulfur species and passivating layer. In addition, a certain surface area of carbon host is required to initiate the nucleation of sulfur species. Nevertheless, the exact mechanism still needs further investigation for a precise control of the growth pathway of sulfur species and its application

in high-energy Li-S batteries. We believe that this finding opens a fundamentally new approach of designing high-energy and low-cost Li-S battery technology through controlling sulfur reaction on low-surface-area carbon host materials.

## Methods

**Sulfur electrode preparation.** For MD-Encap-S/CF cathode preparation, sulfur/carbon composite (75S-CF), super P and polyvinylidene fluoride (PVDF) binder at a weight ratio of 8:1:1 were dispersed in *N*-methyl-2-pyrrolidone (NMP) to form a homogeneous slurry that was cast onto Al current foil ( $\sim 2.5 \text{ mg}_{\text{sulfur}} \text{ cm}^{-2}$ ,  $9/16''$  in diameter). Sulfur/carbon composite 75S-CF was obtained by mixing sulfur and CF at a weight ratio of 75:25 and then heating the mixture at 155 °C overnight.

For  $\text{Li}_2\text{S}_8$  catholyte preparation, in a typical process, 1.345 g of sulfur and 0.275 g of  $\text{Li}_2\text{S}_8$  were added into 1,3-dioxolane (DOL)/1,2-dimethoxyethane (DME) co-solvent (1:1 in volume) with 2 wt %  $\text{LiNO}_3$  additive in a 10 ml volumetric flask. The suspension was heated at 80 °C overnight in an Ar-filled glove box to yield 4.8 M  $\text{Li}_2\text{S}_8$  catholyte with red-brown colour. 1 M, 1.6 M and 2.4 M  $\text{Li}_2\text{S}_8$  in DOL:DME (1:1 in volume), 1 M  $\text{Li}_2\text{S}_8$  in TMS and 1 M  $\text{Li}_2\text{S}_8$  DMSO were obtained according to the same approach. (The concentration of  $\text{Li}_2\text{S}_8$  is based on elemental S.)

For Non-Encap-S/CF cathode preparation, 40 mg carbon nanofibre was dispersed into 40 ml of anhydrous *N,N*-dimethylformamide (DMF) assisted by sonication for 4 h. The obtained suspension was collected to form a free-standing CF sheet via vacuum filtration. The CF sheet was then punched into a  $5/8''$  disc ( $2\text{--}2.5 \text{ mg}$  per piece) and dried at 60 °C in a vacuum overnight. Thirty microlitres of 4.8 M  $\text{Li}_2\text{S}_8$  catholyte (with mass of S equal to 4.6 g and areal loading equal to  $2.32 \text{ mg}_{\text{sulfur}} \text{ cm}^{-2}$ ) was uniformly dropped onto the CF disc and then a coin cell was assembled with the  $\text{Li}_2\text{S}_8$ /CF disc using Li-metal as the counter electrode. The Non-Encap-S/CF electrode was obtained through the initial in situ electrochemical reduction process of the  $\text{Li}_2\text{S}_8$ /CF|Li cell. For long-term cycling of Non-Encap-S/CF electrodes, 10 wt % PVDF binder was added to the CF electrodes and cast onto Al foil ( $9/16''$ ) to enhance the mechanical strength of electrodes.

For  $\text{O}_2$ -plasma-treated CF, the CF sheets were placed into the plasma chamber (Harrick Plasma) at a pressure below 60 m torr to remove the air from the chamber by introducing  $\text{O}_2$  gas first. The  $\text{O}_2$  gas was turned on until a pressure of 550 m torr. The RF power (29.6 W) was then turned on for a specified amount of time of 20 min.

**Electrochemical measurements and characterization.** To evaluate the electrochemical performance of CF electrodes, 2032-type coin cells were assembled using Li metal as the counter electrode, and Celgard 3501 as the separator. MD-Encap-S/CF and Non-Encap-S/CF electrodes were used as cathodes respectively. The electrolyte was a freshly prepared 0.5 M or 1 M lithium bis(trifluoromethanesulfonyl)imide (LiTFSI) in DOL:DME (1:1 in volume) containing 2 wt %  $\text{LiNO}_3$ . Volumes of 40  $\mu\text{l}$  and 10  $\mu\text{l}$  electrolytes were used for the MD-Encap-S/CF and Non-Encap-S/CF cells respectively. Note, the overall electrolyte amounts for both the MD-Encap-S/CF and Non-Encap-S/CF electrodes are the same value of 40  $\mu\text{l}$ . For the Non-Encap-S/CF electrode, 30  $\mu\text{l}$  4.8 M  $\text{Li}_2\text{S}_8$  catholyte was first dropped onto a CF sheet and 10  $\mu\text{l}$  electrolyte was then added within the same cell. The cells were operated in a voltage range of 1.8–2.6 V using a LANHE battery tester. Electrochemical impedance spectra were performed using the Solartron Analytical 1287 Electrochemical interface (4M–5 m Hz). Scanning electron microscopy (SEM) morphology studies of the sulfur electrodes

were conducted on a helium ion microscope. The sulfur electrodes for SEM were briefly rinsed with DME solvent to remove residual salt and avoid destroying the morphology of nucleated sulfur species. X-ray diffraction measurements were performed using a Rigaku MiniFlex II diffractometer with Cu K radiation ( $\lambda=1.5406 \text{ \AA}$ ). X-ray photoelectron spectroscopy (XPS) measurements were performed on a Physical Electronics Quantera Scanning X-ray Microprobe. This system uses a focused monochromatic Al K $\alpha$  X-ray (1,486.7 eV) source for excitation and a spherical section analyser. The XPS data were fitted by CasaXPS software using Gaussian/Lorentzian line shape and Shirley background correction.

**Classical molecular dynamics simulation.** Classical molecular dynamics (MD) was performed using GROMACS MD simulation package version 5.1.2. for the electrolytes of 0.25 M Li<sub>2</sub>S, 1 M LiTFSI in TMS, DOL, DME and DMSO solvent separately<sup>44</sup>. The molecules are initially packed randomly in a cubic box of size 60×60×60 Å<sup>3</sup> periodic in the XYZ direction using PACKMOL<sup>45</sup>. The initial configuration is minimized in two steps, first using steepest descent employing a convergence criterion of 1,000 kcal mol<sup>-1</sup> Å<sup>-1</sup>, and then conjugated-gradient energy minimization scheme employing a convergence criterion of 10 kcal mol<sup>-1</sup> Å<sup>-1</sup>. The systems were equilibrated in the isothermal-isobaric ensemble (constant NPT) using the Berendsen barostat to maintain the pressure of 1 bar with a time constant of 2 ps for 2 ns (ref. <sup>46</sup>). All systems were then melted at 400 K for 2 ns and subsequently annealed from 400 to 298 K in three steps for 3 ns. Finally, the production runs of 20 ns were then obtained in the canonical ensemble (NVT) using an improved velocity-rescaling algorithm proposed by in the literature with a time constant of 0.1 ps at 298 K (ref. <sup>46</sup>). The simulation time was long enough to sample adequately the Fickian (diffusive) regime of all systems and the results were averaged over at least two independent realizations of the same system. The bonded and non-bonded parameters for TMS, DOL, DME and DMSO are taken from the general AMBER force field, and those for TFSI<sup>-</sup> anions, lithium cations and polysulfide anions are from previous reports<sup>47,48</sup>. The partial atomic charges for all molecules were derived by first optimizing the geometry using Becky's three-parameter exchange function combined with the Lee–Yang–Parr correlation functional (B3LYP) at the aug-cc-pvdz theory level using the Gaussian 09<sup>49</sup> package and then fitting the electrostatic potential surface using the RESP method. Long-range electrostatic interactions were handled by the particle-mesh Ewald method with a grid spacing of 0.1 nm. The cutoff distance of 1.2 nm was used for electrostatic and Lennard-Jones interactions. Other simulation details are very close to our previous publication<sup>50</sup>.

**NMR measurement.** Li<sup>+</sup> cation diffusion coefficients were determined using <sup>7</sup>Li pulsed field gradient NMR on a 600 MHz NMR spectrometer (Agilent) equipped with a 5 mm liquid NMR probe (Doty Scientific) that has a maximum  $z$ -gradient strength of  $\sim 31 \text{ T m}^{-1}$ . The <sup>7</sup>Li stimulated echo profiles were obtained using the pulse sequence with bipolar gradients (Dbpppste; Vender supplied, Vnmrj) as a function of gradient strength ( $g$ ) and fitted with the Stejskal–Tanner equation

$$S(g) = S(0)e^{-D(\gamma g \delta)^2 (\Delta - (\delta/3))}$$

where  $S(g)$  and  $S(0)$  are the echo height at the gradient strength of  $g$  and 0, respectively,  $D$  is the diffusion coefficient,  $\gamma$  is the gyromagnetic ratio of <sup>7</sup>Li,  $\Delta$  is the diffusion delay and  $\delta$  is the gradient length. For these samples,  $\delta$  and  $\Delta$  are fixed at 2 and 30 ms, respectively and  $g$  was varied in 16 equal steps. The maximum gradient strength was chosen carefully for a sufficient decay of echo profiles.

**Data availability.** The data that support the plots within this paper and other findings of this study are available from the corresponding author upon reasonable request.

Received: 11 April 2017; Accepted: 1 August 2017;  
Published online: 25 September 2017

## References

- Bruce, P. G., Freunberger, S. A., Hardwick, L. J. & Tarascon, J.-M. Li–O<sub>2</sub> and Li–S batteries with high energy storage. *Nat. Mater.* **11**, 19–29 (2012).
- Ji, X., Lee, K. T. & Nazar, L. F. A highly ordered nanostructured carbon–sulphur cathode for lithium–sulphur batteries. *Nat. Mater.* **8**, 500–506 (2009).
- Manthiram, A., Chung, S.-H. & Zu, C. Lithium–sulfur batteries: Progress and prospects. *Adv. Mater.* **27**, 1980–2006 (2015).
- Eroglu, D., Zavadil, K. R. & Gallagher, K. G. Critical link between materials chemistry and cell-level design for high energy density and low cost lithium–sulfur transportation battery. *J. Electrochem. Soc.* **162**, A982–A990 (2015).
- Hagen, M. et al. Lithium–sulfur cells: The gap between the state-of-the-art and the requirements for high energy battery cells. *Adv. Energy Mater.* **5**, 1401986 (2015).
- Adv. Energy Mater. **5**, 1402290 (2015).
- Mikhaylik, Y. V. & Akridge, J. R. Polysulfide shuttle study in the Li/S battery system. *J. Electrochem. Soc.* **151**, A1969–A1976 (2004).
- Aurbach, D. et al. On the surface chemical aspects of very high energy density, rechargeable Li–sulfur batteries. *J. Electrochem. Soc.* **156**, A694–A702 (2009).
- Yang, Y. et al. High-capacity micrometer-sized Li<sub>2</sub>S particles as cathode materials for advanced rechargeable lithium-ion batteries. *J. Am. Chem. Soc.* **134**, 15387–15394 (2012).
- Meini, S., Elazari, R., Rosenman, A., Garsuch, A. & Aurbach, D. The use of redox mediators for enhancing utilization of Li<sub>2</sub>S cathodes for advanced Li–S battery systems. *J. Phys. Chem. Lett.* **5**, 915–918 (2014).
- Schuster, J. et al. Spherical ordered mesoporous carbon nanoparticles with high porosity for lithium–sulfur batteries. *Angew. Chem. Int. Edn* **51**, 3591–3595 (2012).
- Zhang, C., Wu, H. B., Yuan, C., Guo, Z. & Lou, X. W. Confining sulfur in double-shelled hollow carbon spheres for lithium–sulfur batteries. *Angew. Chem.* **124**, 9730–9733 (2012).
- Cao, Y. et al. Sandwich-type functionalized graphene sheet–sulfur nanocomposite for rechargeable lithium batteries. *Phys. Chem. Chem. Phys.* **13**, 7660–7665 (2011).
- Zhou, G. et al. A graphene–pure-sulfur sandwich structure for ultrafast, long-life lithium–sulfur batteries. *Adv. Mater.* **26**, 625–631 (2014).
- Zheng, G., Yang, Y., Cha, J. J., Hong, S. S. & Cui, Y. Hollow Carbon nanofiber-encapsulated sulfur cathodes for high specific capacity rechargeable lithium batteries. *Nano Lett.* **11**, 4462–4467 (2011).
- Zheng, G. et al. Amphiphilic surface modification of hollow carbon nanofibers for improved cycle life of lithium sulfur batteries. *Nano Lett.* **13**, 1265–1270 (2013).
- Wei Seh, Z. et al. Sulphur–TiO<sub>2</sub> yolk–shell nanoarchitecture with internal void space for long-cycle lithium–sulphur batteries. *Nat. Commun.* **4**, 1331 (2013).
- Pang, Q., Kundu, D., Cuisinier, M. & Nazar, L. F. Surface-enhanced redox chemistry of polysulphides on a metallic and polar host for lithium–sulphur batteries. *Nat. Commun.* **5**, 4759 (2014).
- Xiao, L. et al. A soft approach to encapsulate sulfur: polyaniline nanotubes for lithium–sulfur batteries with long cycle life. *Adv. Mater.* **24**, 1176–1181 (2012).
- Chen, H. et al. Rational design of cathode structure for high rate performance lithium–sulfur batteries. *Nano Lett.* **15**, 5443–5448 (2015).
- Song, J., Yu, Z., Gordin, M. L. & Wang, D. Advanced sulfur cathode enabled by highly crumpled nitrogen-doped graphene sheets for high-energy-density lithium–sulfur batteries. *Nano Lett.* **16**, 864–870 (2016).
- Fan, Q., Liu, W., Weng, Z., Sun, Y. & Wang, H. Ternary hybrid material for high-performance lithium–sulfur battery. *J. Am. Chem. Soc.* **137**, 12946–12953 (2015).
- Sun, Q. et al. An aligned and laminated nanostructured carbon hybrid cathode for high-performance lithium–sulfur batteries. *Angew. Chem. Int. Edn* **54**, 10539–10544 (2015).
- Manthiram, A., Fu, Y. & Su, Y.-S. Challenges and prospects of lithium–sulfur batteries. *Acc. Chem. Res.* **46**, 1125–1134 (2012).
- Yao, H. et al. Improved lithium–sulfur batteries with a conductive coating on the separator to prevent the accumulation of inactive S-related species at the cathode–separator interface. *Energy Environ. Sci.* **7**, 3381–3390 (2014).
- Yao, H. et al. Improving lithium–sulphur batteries through spatial control of sulphur species deposition on a hybrid electrode surface. *Nat. Commun.* **5**, 3943 (2014).
- Xu, R. et al. Insight into sulfur reactions in Li–S batteries. *ACS Appl. Mat. Interfaces* **6**, 21938–21945 (2014).
- Fan, F. Y. et al. Polysulfide flow batteries enabled by percolating nanoscale conductor networks. *Nano Lett.* **14**, 2210–2218 (2014).
- Zheng, J. et al. Controlled nucleation and growth process of Li<sub>2</sub>S<sub>2</sub>/Li<sub>2</sub>S in lithium–sulfur batteries. *J. Electrochem. Soc.* **160**, A1992–A1996 (2013).
- Aetukuri, N. B. et al. Solvating additives drive solution-mediated electrochemistry and enhance toroid growth in non-aqueous Li–O<sub>2</sub> batteries. *Nat. Chem.* **7**, 50–56 (2015).
- Gao, X., Chen, Y., Johnson, L. & Bruce, P. G. Promoting solution phase discharge in Li–O<sub>2</sub> batteries containing weakly solvating electrolyte solutions. *Nat. Mater.* **15**, 882–888 (2016).
- Fan, F. Y., Carter, W. C. & Chiang, Y.-M. Mechanism and kinetics of Li<sub>2</sub>S precipitation in lithium–sulfur batteries. *Adv. Mater.* **27**, 5203–5209 (2015).
- Liu, T. et al. Cycling Li–O<sub>2</sub> batteries via LiOH formation and decomposition. *Science* **350**, 530–533 (2015).
- Cañas, N. A. et al. Investigations of lithium–sulfur batteries using electrochemical impedance spectroscopy. *Electrochim. Acta* **97**, 42–51 (2013).
- Deng, Z. et al. Electrochemical impedance spectroscopy study of a lithium/sulfur battery: modeling and analysis of capacity fading. *J. Electrochem. Soc.* **160**, A553–A558 (2013).
- Fan, F. Y. & Chiang, Y.-M. Electrodeposition kinetics in Li–S batteries: Effects of low electrolyte/sulfur ratios and deposition surface composition. *J. Electrochem. Soc.* **164**, A917–A922 (2017).

37. Estevez, L. et al. Tunable oxygen functional groups as electrocatalysts on graphite felt surfaces for all-vanadium flow batteries. *ChemSusChem* **9**, 1455–1461 (2016).
38. Pang, Q., Liang, X., Kwok, C. Y. & Nazar, L. F. Advances in lithium–sulfur batteries based on multifunctional cathodes and electrolytes. *Nat. Energy* **1**, 16132 (2016).
39. Cataldo, F. A revision of the Gutmann donor numbers of a series of phosphoramides including TEPA. *Eur. Chem. Bull.* **4**, 92–97 (2015).
40. Thanh, N. T. K., Maclean, N. & Mahiddine, S. Mechanisms of nucleation and growth of nanoparticles in solution. *Chem. Rev.* **114**, 7610–7630 (2014).
41. Johnson, L. et al. The role of LiO<sub>2</sub> solubility in O<sub>2</sub> reduction in aprotic solvents and its consequences for Li–O<sub>2</sub> batteries. *Nat. Chem.* **6**, 1091–1099 (2014).
42. Bijani, S. et al. Study of the Nucleation and growth mechanisms in the electrodeposition of micro- and nanostructured Cu<sub>2</sub>O thin films. *J. Phys. Chem. C* **115**, 21373–21382 (2011).
43. Wei, C., Wu, G., Yang, S. & Liu, Q. Electrochemical deposition of layered copper thin films based on the diffusion limited aggregation. *Sci. Rep.* **6**, 34779 (2016).
44. Abraham, M. J., van der Spoel, D., Lindahl, E., Hess, B. & GROMACS Development Team. *GROMACS User Manual version 5.1.2*. GROMACS User Manual v.5.1.2 (2016); [www.gromacs.org](http://www.gromacs.org).
45. Martínez, L., Andrade, R., Birgin, E. G. & Martínez, J. M. Packmol: A package for building initial configurations for molecular dynamics simulations. *J. Comput. Chem.* **30**, 2157–2164 (2009).
46. Bussi, G., Zykova-Timan, T. & Parrinello, M. Isothermal-isobaric molecular dynamics using stochastic velocity rescaling. *J. Chem. Phys.* **130**, 074101 (2009).
47. Takeuchi, M. et al. Ion–ion interactions of LiPF<sub>6</sub> and LiBF<sub>4</sub> in propylene carbonate solutions. *J. Mol. Liq.* **148**, 99–108 (2009).
48. Rajput, N. N. et al. Elucidating the solvation structure and dynamics of lithium polysulfides resulting from competitive salt and solvent interactions. *Chem. Mater.* **29**, 3375–3379 (2017).
49. Frisch, M. et al. *Gaussian 09* (Gaussian Inc., Wallingford, CT, 2009).
50. Rajput, N. N., Qu, X., Sa, N., Burrell, A. K. & Persson, K. A. The coupling between stability and ion pair formation in magnesium electrolytes from first-principles quantum mechanics and classical molecular dynamics. *J. Am. Chem. Soc.* **137**, 3411–3420 (2015).

### Acknowledgements

This work was supported as part of the Joint Center for Energy Storage Research (JCESR), an Energy Innovation Hub funded by the US Department of Energy (DOE), Office of Science, Basic Energy Sciences (BES). The SEM images, XPS and NMR measurements were performed at the Environmental Molecular Sciences Laboratory (EMSL), a national scientific user facility sponsored by the US Department of Energy's Office of Biological and Environmental Research and located at Pacific Northwest National Laboratory (PNNL). PNNL is operated by Battelle for the Department of Energy under Contract DE-AC05-76RLO1830.

### Author contributions

H.P., Y.S. and J.L. conceived the research. H.P., Y.S., J.L. and Y.C. designed the experiments. H.P., J.C., R.C. and L.E. performed the experiments and measurements. V.M., K.H. and K.T.M. performed NMR. N.N.R. and K.P. performed MD simulation. M.H.E. performed XPS analysis. All authors discussed the results. K.P., J.-G.Z., K.T. and Y.C. revised the manuscript. H.P., Y.S. and J.L. wrote the paper with input from all authors.

### Competing interests

The authors declare no competing financial interests.

### Additional information

**Supplementary information** is available for this paper at doi:10.1038/s41560-017-0005-z.

**Reprints and permissions information** is available at [www.nature.com/reprints](http://www.nature.com/reprints).

**Correspondence and requests for materials** should be addressed to Y.S. or J.L.

**Publisher's note:** Springer Nature remains neutral with regard to jurisdictional claims in published maps and institutional affiliations.